npj | computational materials

Article

Published in partnership with the Shanghai Institute of Ceramics of the Chinese Academy of Sciences

https://doi.org/10.1038/s41524-024-01315-5

Probing phonon focusing, thermomechanical behavior, and moiré patterns in van der Waals architectures using surface acoustic waves

Nitish Baradwaj[1], Anikeya Aditya[1], Ankit Mishra[1], Kory Burns[2], Eric Lang[3], Jordan A. Hachtel[4], Khalid Hattar[5], Assel Aitkaliyeva[6], Aiichiro Nakano[1], Priya Vashishta[1] & Rajiv Kalia[1] ✉

Surface acoustic waves (SAWs) propagate along solid-air, solid-liquid, and solid-solid interfaces. Their characteristics depend on the elastic properties of the solid. Combining transmission electron microscopy (TEM) experiments with molecular dynamics (MD) simulations, we probe atomic environments around intrinsic defects that generate SAWs in vertically stacked two-dimensional (2D) bilayers of MoS_2. Our joint experimental-simulation study provides insights into SAW-induced structural and dynamical changes and thermomechanical responses of MoS_2 bilayers. Using MD simulations, we compute mechanical properties from the SAW velocity and thermal conductivity from thermal diffusion of SAWs. The results for Young's modulus and thermal conductivity of an MoS_2 monolayer are in good agreement with experiments. The presence of defects, such as nanopores which generate SAWs, reduces the thermal conductivity of 2D-MoS_2 by an order of magnitude. We also observe dramatic changes in moiré patterns, phonon focusing, and cuspidal structures on 2D-MoS_2 layers.

Two-dimensional (2D) van der Waals (vdW) materials, renowned for their exceptional electronic, magnetic, and thermal properties, as well as their large relative surface areas, hold immense potential for integration with surface acoustic waves (SAWs). This integration presents opportunities for diverse applications spanning quantum information, sensing, and microfluidics applications[1,2]. The predominant focus of current research lies in exploring the integration of SAWs with plasmonic coupling[3] and acoustic charge transport in graphene[4]. Research has also delved into the piezoelectric coupling of SAWs with charge carriers in other 2D material systems[5–7]. On the contrary, scant attention has been given to investigating the distortions arising from the mechanical coupling and interactions between SAWs and defect centers. This aspect bears particular significance for the integration of 2D materials and SAW devices as the properties of as-fabricated materials are largely determined by their structure and intrinsic defects. These defects can arise during sample preparation (e.g., grain boundaries or isolated vacancies and antisite defects) or transfer processes (e.g., wrinkles and tears)[8], underscoring the need for comprehensive exploration of their effects on devices. Previous studies have shown that defects can be used to tune properties[9–12], control strain[8], and induce moiré patterns in 2D transition metal dichalcogenides[13,14]. However, further work is imperative to elucidate the intricate relationship between intrinsic defects, SAWs, and material properties.

Here, rather than focusing on integrating 2D materials with SAW devices, we introduce a methodology for monitoring the propagation of SAWs on 2D materials. This approach combines experimental techniques with simulation and machine learning to advance our understanding of SAW dynamics on such materials. SAW propagation is contingent upon material properties in the vicinity of the surface, making SAW an excellent tool for exploring thermomechanical properties of 2D layers. The longitudinal and transverse components of the SAWs interact with the 2D MoS_2 layers and are influenced by defects on the MoS_2 surfaces.

There are two ways to determine elastic constants: static and dynamic. Papadakis[15] describes a non-destructive method for determining Young's modulus (E) and Poisson's ratio (ν) through the measurement of shear and

[1]Collaboratory for Advanced Computing and Simulations, University of Southern California, Los Angeles, CA, USA. [2]Department of Materials Science & Engineering, University of Virginia, Charlottesville, VA, USA. [3]Department of Nuclear Engineering, University of New Mexico, Albuquerque, NM, USA. [4]Center for Nanophase Materials Sciences, Oak Ridge National Laboratory, Oak Ridge, TN, USA. [5]Department of Nuclear Engineering, University of Tennessee, Knoxville, TN, USA. [6]Department of Materials Science & Engineering, University of Florida, Gainesville, FL, USA. ✉e-mail: rkalia@usc.edu

longitudinal velocities. Another method involves measuring the resonance frequencies of a slender bar to determine elastic constants, where SAWs are generated by a piezoelectric transducer. SAWs can also be generated by methods such as surface impact or the wedge technique, and they can be detected using transducers or laser interferometry[16–18].

Bayón et al. [19] have estimated elastic constants through measurements of SAW velocity, the ratio of normal to the longitudinal displacement components, and the material density. Their approach necessitates the detection of a single wave pulse at a specific point on a surface to measure both the SAW velocity and the ratio of the normal to the longitudinal displacement within the SAW. They find that the dimensionless quantity, $B = \frac{E}{\rho V^2}$, where E the Young's modulus and ρ and V are the mass density and SAW velocity, respectively, can be fitted to

$$B = 2.618 + 1.33\nu, \tag{1}$$

for $\nu \in [0, 0.5]$. The Young's modulus of a material supporting SAW can be calculated from the measured SAW velocity and the solid's Poisson's ratio using Eq. (1).

Four-dimensional electron microscopy has been employed to visualize the generation and propagation of SAWs in a thin semiconducting polymeric film (P3HT). The mechanical behavior of the polymer has been characterized through the SAW dynamics using the equation[20],

$$B = \frac{2(1+\nu)^3}{(0.87+1.12\nu)^2} \tag{2}$$

Equations (1) and (2) are very close to the exact solution derived by Malischewsky and Tuan[21] (see supplementary information).

Because SAWs are confined to the surface[22], their velocity and amplitude offer insights into the effects of surface defects on material properties, enabling the establishment of defect-property relationships. We employ atomistic-level SAW modeling to determine thermomechanical properties and explore how phonon-focusing features of SAWs alter moiré patterns in MoS_2 bilayers. These simulations are complemented by electron microscopy and optical spectroscopy data to confirm the influence of SAWs on lattice environments and phonon density of states. Our findings reveal that point sources of SAW generation significantly impact the phonon density of states and thermal transport on 2D-MoS_2 surfaces, unveiling remarkable phonon-focusing features and cuspidal structures resulting from internal diffractions of SAWs[23]. Ultimately, we demonstrate the potential for SAWs to couple with defect centers, offering a promising technique for directly tuning emission energies in vdW solids.

Methods

Experimental methods

In this study, two different preparation techniques for MoS_2 are being utilized. First, free-standing sheets are prepared by subjecting monolayer MoS_2 powder to sonication submerged in N, N-dimethylformamide (DMF) at a concentration of 15 mg ml^{-1}. The sample is sonicated for 1.5 hours to aid in the separation of the flakes based on density and then drop-casted onto holey carbon TEM grids for analysis. Samples on the sapphire substrate are grown by a CVD method, described in more detail here[24]. The ex-situ irradiations are conducted on previously prepared substrate-supported and free-standing MoS_2 flakes, as described above. The specimens are subjected to a broad beam of 15 MeV Au^{4+} ions at room temperature using a 6 MV HVEE EN tandem accelerator. The ion fluence remains constant at 1×10^{13} cm^{-2} and the angle of incidence remains at 60° to align the sample geometry with the ion beam.

Raman spectroscopy is collected on a Horiba Jobin-Yvon LabRam ARAMIS micro-Raman with an excitation wavelength of 532 nm, ×100 objective lens, neutral density filter with 50% transparency to prevent local heating effects and minimize thermal damage, and a cooled CCD detector. All spectra are acquired at 298 K (±2 K). Measurements are conducted using an 1800 g mm^{-1} grating. STEM images are acquired with an aberration corrected UltraSTEM 100 operated at an accelerating voltage of 60 kV. The experiments are performed with a convergence semi angle of 30 mrad.

Simulation methods

Molecular dynamics. Molecular dynamics (MD) simulations are performed using a Stillinger-Weber type forcefield (SWFF). The forcefield parameters are calibrated using data derived from Density Functional Theory (DFT) simulations, tailored to match the thermomechanical properties and phonon dispersions of 2D-MoS_2 under ambient conditions, with both tensile and compressive loadings[25–28].

MD simulations are performed to gain insight into the propagation of SAW in MoS_2 bilayers. The system comprises two monolayers of MoS_2, with the bottom layer measuring 300×300 nm^2 and featuring a 15 nm pore at its center under periodic boundary conditions. The top layer, with dimensions of 200×200 nm^2, remains pristine. The smaller size facilitates the rotation of the top layer to investigate the effects of relative rotation on SAW propagation. In total, the system consists of 4,541,310 atoms. The simulations are performed in the NVT ensemble at 77 K (liquid nitrogen temperature). In separate simulations, we rotate the top sheet by angles of 0.5°, 5°, 15°, and 30°.

Convolutional neural network. The computational cost of classifying structural transformations between 2H and 1T crystalline phases, along with defects, becomes significant for large systems comprising millions of atoms. To tackle this challenge, we employ a convolutional neural network (CNN), renowned for its efficiency and precision in capturing the intricate details of phase transformations and defect distribution in MoS_2 monolayer and bilayers.

We train the CNN by transforming atomic coordinates into image-based data. The input data comprises patches measuring 14×14 $Å^2$ centered around each Mo atom. These patches are converted into $64 \times 64 \times 3$ tensors using a grid of size 0.3×0.3 $Å^2$. The atomic coordinates are transformed into a tensor using an exponential kernel,

$$T_{c=1,2,3}(x,y) = \sum_{i=1}^{N} \exp\left(-\frac{(x-x_i)^2+(y-y_i)^2}{\eta^2}\right) \tag{3}$$

where c refers to the input channel, (x, y) corresponds to the center of a grid, (x_i, y_i) are the coordinates of Mo and S atoms, and N is the total number of atoms within a 14×14 $Å^2$ patch around the central Mo atom. The width of the exponential kernel η is chosen to be 0.2 Å.

The CNN architecture includes three convolutional layers with dimensions $32 \times 32 \times 32$, $64 \times 16 \times 16$, and $64 \times 8 \times 8$, along with two fully connected layers featuring 4096 and 10 units. At the end, a softmax layer outputs a number corresponding to 2H, 1T, and various defects. Further details are provided in the supplementary information.

Results and discussion

The results are delineated into three sections: (1) Generation of surface acoustic waves (SAWs) in bilayers through nanopores; (2) analysis of thermomechanical response of monolayers influenced by SAWs; and (3) observations of SAW-induced moiré patterns in bilayers.

SAWs generation in bilayers through nanopores

This experimental study builds upon our previous work[13], where a high-angle ion beam irradiates a bilayer sheet of MoS_2 relative to the sample. The impinging ion approaches the grazing angle of incidence, resulting in a non-uniform defect concentration between the top and bottom sheets. We leverage this phenomenon to elucidate the origin of moiré pattern generation in the present study. Figure 1a is a series of atomic-resolution high-angle annular dark field (HAADF) scanning transmission electron microscopy (STEM) micrographs of bilayer MoS_2 sheets, where the rotation angle is generated from a lattice mismatch between vertically aligned sheets of

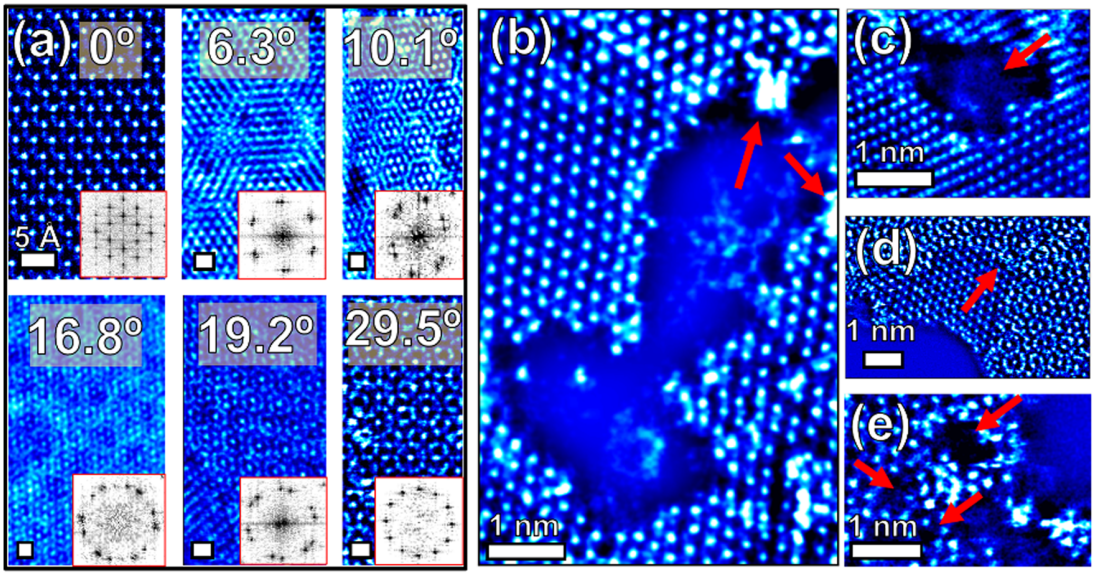

Fig. 1 | HAADF-STEM images of irradiated single and bilayer sheets of MoS2. All scale bars represent 5Å. **a** Bilayer crystals of MoS2 with rotational misalignments ranging between 0° and 30°. Insets represent FFTs of each real space image. **b**–**e** represent disordered crystals with red arrows highlighting vacancy clusters and defective areas.

MoS_2. The displacement source generating various misorientation angles comprises defects induced by an ion beam stimulus.

In increments of ~5°, moiré patterns are shown from STEM images from 0° to 30° (except for 25° since the periodicity is nearly identical to 20°). The fast Fourier transforms (FFTs) are reciprocal space vectors of the corresponding STEM images shown in the inset of each figure. The rotational misalignment is calculated by examining the angle between diffraction peaks within the 1st Brillouin zone (BZ). Here, 0° is an epitaxial bilayer crystal with AB stacking and 30° is the maximum possible offset of two hexagonal lattices. In Fig. 1b–e, we observe various types of disorder resulting from the ion beam, highlighted by the red arrows. In Fig. 1b, a large extended nanopore is displayed with some Mo clusters binding to the edges of the pore, highlighted with red arrows. Figure 1c depicts a nanometer-sized pore surrounded by a 3R-MoS_2 region, where the deformation fields likely contribute to the formation of the less energetically favorable polymorph. Figure 1d is an etched region of the top layer of the sheet, with a misoriented grain in the surrounding region. In Fig. 1e, we observe sub-nanometer-sized vacancy clusters scattered throughout the lattice. In each case, the atomic environment is depleted of S atoms because of their preferential sputtering (verified from SRIM simulations[29] and first principles calculations[8]).

Our simulations reveal that defects such as nanopores in irradiated 2D-MoS_2 systems generate SAWs. These waves exhibit longitudinal and transverse components, each associated with distinct velocities. Those components manifest in in-plane and out-of-plane displacements of atoms. We determine the frequency of the SAW by analyzing the transverse displacements of the MoS_2 layer that encompasses the nanopore. The frequency is 3.762 GHz. Notably, the SAW frequency remains almost unchanged between the pristine layer and the layer containing the nanopore.

Figure 2 illustrates MD results for out-of-plane atomic displacements, representing SAW amplitudes after the waves have traversed the top (left column) and bottom (right column) layers. Panels in the left column depict anisotropic SAW amplitudes (indicated by yellow and red lines) resulting from surface phonon focusing on the top layer. This striking feature persists irrespective of whether the top layer is perfectly aligned with the bottom layer or rotated through twist angles $\theta = 0.5°$, 5°, 15°, or 30°. Additionally, phonon focusing is observed to a lesser extent, in the bottom layer at small twist angles (≤5°). While it may initially appear counterintuitive for isotropic material like the 2D-MoS_2 to exhibit phonon focusing, it is important to note that strains in the system are anisotropic (Fig. S5) due to the anisotropy of the nanopore. This anisotropy gives rise to SAW-induced phonon focusing (refer to Fig. S3). Figure 2 illustrates that phonon-focusing features on the two layers are not aligned, resulting in a slight twist between the monolayers, as is also observed in our TEM experiments shown in Fig. 1.

Panels in the left column of Fig. 2 highlight another notable feature of SAWs: cusps in the top layer (indicated by kinks in the blue circling contours)[23]. Surprisingly, cusps are not as pronounced in the SAW footprint on the bottom layer. Panels (e)–(g) show how the twist angle affects phonon focusing and cuspidal structure. In panels (c) and (d), the SAW amplitudes in the top and bottom layers at $\theta = 0.5°$ indicate phonon focusing remains prominent, although the focusing directions have shifted compared to those in perfectly aligned layers (Fig. 2a, b). Cusps persist on the top but not the bottom layer when the twist angle is increased to 5°, 15°, or 30°; refer to Fig. 2e–j.

Experiments and theoretical calculations consistently highlight cuspidal structures as fundamental features of phonon focusing during SAW propagation on surfaces[30]. Cusps have been observed on surfaces of Si and other materials[30]. Experimentally, these structures arise only when SAWs originate from point-like sources generated by surface ablation using a laser beam. Multiple SAWs have been experimentally detected in cusp regions; a phenomenon replicated in our simulations (refer to the movie in supplementary section VII). Additionally, cusps are observed when SAWs are generated from multiple nanopores.

Thermomechanical response of monolayers to SAWs

From the snapshots in Fig. 2, we can track the dynamics of the SAW wavefront and compute the SAW velocity in both the top and bottom MoS_2 layers. Remarkably, the SAW velocity remains nearly constant in both layers (3600 m s^{-1}), regardless of the twist angle of the bilayer. Using the average SAW velocity and the Poisson's ratio (0.38) from our MD calculations, we calculate Young's modulus of the top layer using Eq. (1). The resulting value (247.2 ± 9.2 GPa) is in good agreement with experimental findings[31], 265 ± 13 GPa.

In addition to Young's modulus, we also compute the thermal conductivity, κ, from the SAW dynamics using the formula:

$$\kappa = \alpha C \rho \tag{4}$$

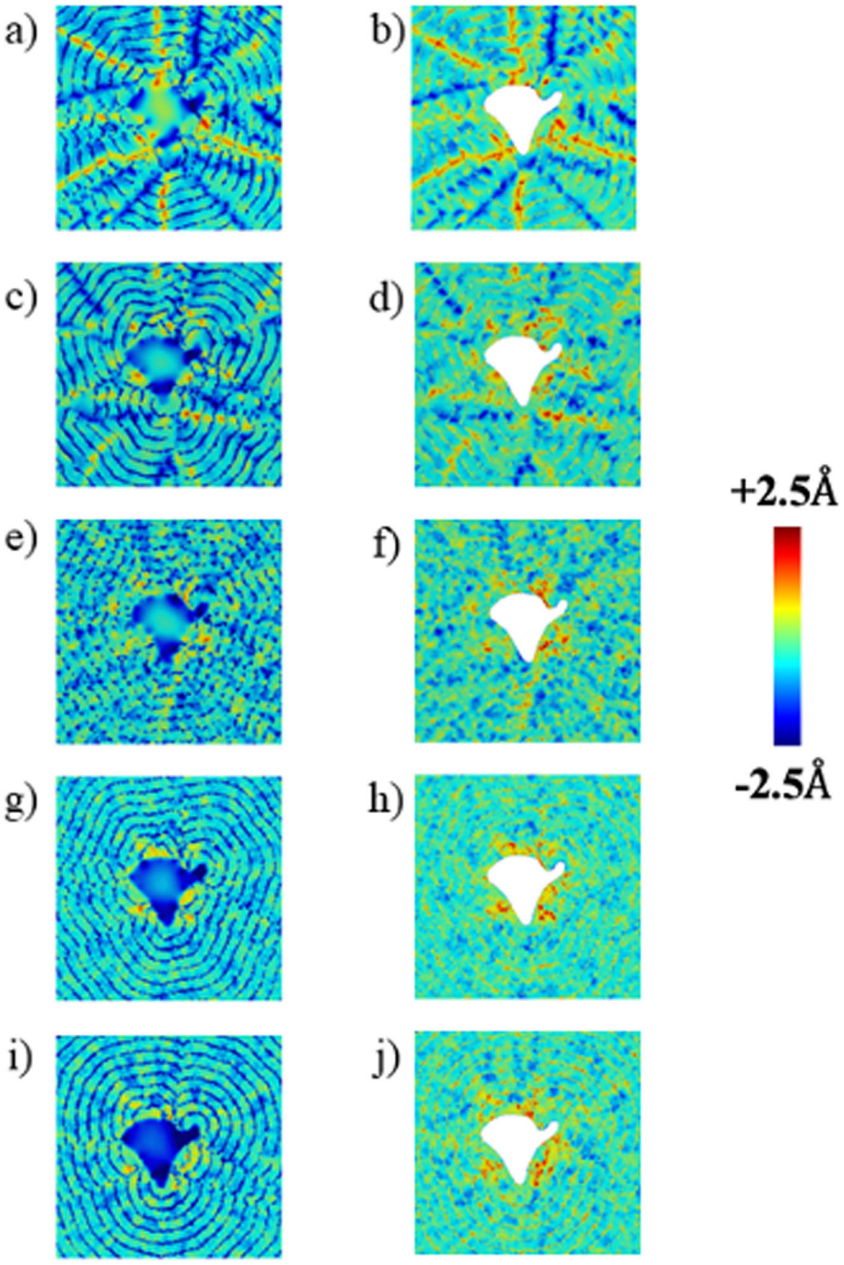

Fig. 2 | Shows out-of-plane atomic displacements in a pristine MoS_2 monolayer (left column) on top of an MoS_2 monolayer with a nanopore (right column). The color bar indicates the range of vertical displacements of atoms. Panels **a** and **b** show the patterns created by the SAW in a system with 0° twist between the monolayers. The red-yellow lines show phonon focusing on the layers. Panels **c** and **d** show that the corresponding patterns start to break at a twist angle of $\theta = 0.5°$. Phonon focusing starts to diminish as the top layer is further rotated relative to the bottom layer; see panels **e** and **f** corresponding to $\theta = 5°$, panels **g** and **h** at $\theta = 15°$, and **i** and **j** at $\theta = 30°$. The rotation does not affect the region in the top layer right above the pore, where the pore is sucked in and the shape of the nanopore can be seen in the top layer. Pixelated images of normal displacements are shown in Fig. S3. They are smaller in magnitude than the atomic displacements in this figure.

where α is the thermal diffusivity associated with the temperature profile accompanying SAW dynamics and ρ and C are the monolayer mass density and heat capacity, respectively. From the MD data for the SAW dynamics on the top layer, we find $\alpha = 0.66 \times 10^{-5}$ m^2 s^{-1} and κ = 19.31 W K^{-1}. m^{-1} at temperature $T = 77$ K. Additionally, we have computed thermal conductivity at several temperatures using direct MD calculations with quantum corrections at low temperatures, as illustrated in Fig. 3a. Remarkably, the thermal conductivity estimate from the SAW dynamics closely aligns with the extrapolated quantum corrected value from the direct MD calculation at 77 K, as shown in Fig. 3.

We also investigate the impact of nanopores on thermal conductivity of an MoS_2 monolayer using direct MD simulations. This involves setting up heat baths in defect-free regions of MoS_2, with nanopores situated between the heat baths. Within that setup, we determine the steady-state temperature gradient and heat flux to directly calculate thermal conductivity using Fourier's law of heat conduction. The results depicted in the right panel of Fig. 3 demonstrate that the thermal conductivity decreases by an order of magnitude in the presence of a single pore measuring 10 nm in size. Furthermore, we explore the effect of smaller randomly distributed nanopores on thermal conductivity, which once again reveals a dramatic decrease compared to the value for the defect-free monolayer.

The precipitous drop in thermal conductivity can be attributed to the phonon density of states, which plays a crucial role in thermal conduction. As illustrated in Fig. 4a, b, the presence of defects such as nanopores induces a substantial change in the phonon density of states, particularly at energies below 30 meV. These low-frequency phonon modes are localized as evidenced by the calculation of the participation ratio,

$$P_\lambda = \frac{1}{N\sum_{i,\alpha}\left(\varepsilon^*_{i\alpha,\lambda}\varepsilon_{i\alpha,\lambda}\right)^2}, \quad (5)$$

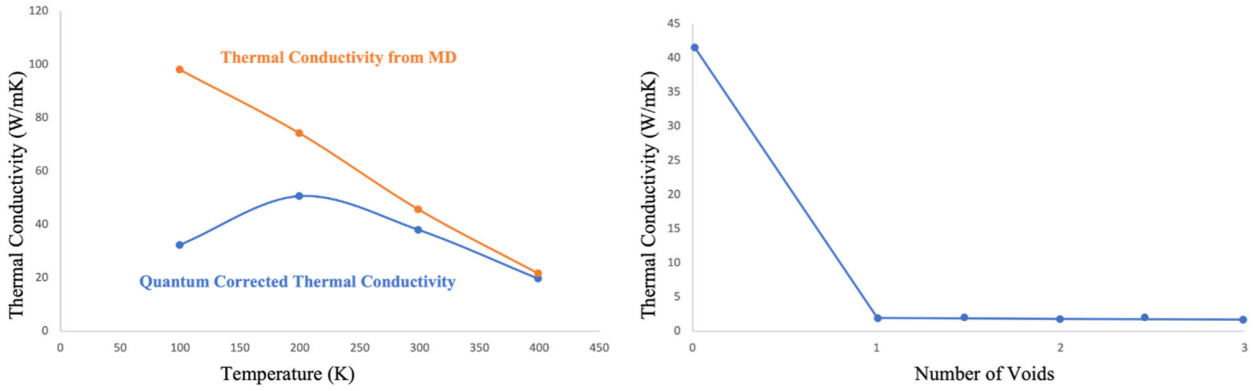

Fig. 3 | The left panel shows the temperature dependence of thermal conductivity *K* for a pristine monolayer of MoS_2 from MD simulations (orange). Also shown are the quantum-corrected values (blue) obtained by multiplying κ with the specific heat which includes quantum corrections[9]. Evidently, the quantum contribution to thermal conductivity is much larger at lower temperatures. The right panel shows thermal conductivity in MoS_2 sheets as a function of number of voids. Thermal conductivity drops by an order of magnitude due to the presence of a single void. The number of voids does not make a difference thereafter.

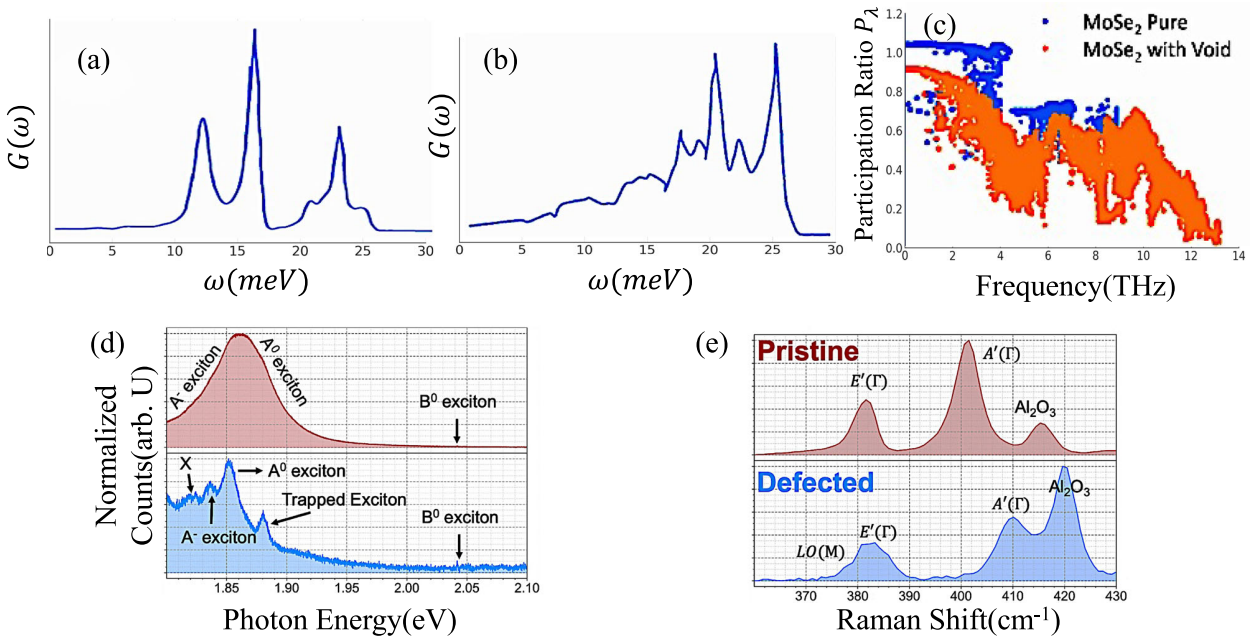

Fig. 4 | Comparison of the density of state, phonon Modes and the spectra of pristine and defected MoS_2 systems. Shows the vibrational density of states and phonon modes of a pristine MoS_2 monolayer (**a**) and that of a MoS_2 monolayer with a single void (**b**). The difference between the two is evident in the low-frequency regime. **c** Shows the phonon participation ratio calculated by MD. The presence of a nanopore suppresses phonons with participation ratio values below 0.4. This behavior is consistent with Anderson's theory of localization of waves in disordered two-dimensional systems driven by interference between multiple wave scattering as well as experimental observations in other two-dimensional materials. **d** and **e** denote the Photoluminescence and Raman spectra of Pristine MoS_2 and defected MoS_2 with a nanopore respectively.

where N is the number of atoms and $\varepsilon_{i\alpha,\lambda}$ is the α^{th} Cartesian component of atom i for the phonon mode of wavelength λ. The participation ratio ranges between 1 for propagating modes and $1/N$ for localized modes. It is apparent from Fig. 4(c) that low-frequency phonon modes below 30 meV are extended in a pristine MoS_2 monolayer, whereas they become localized in the presence of nanopores, as indicated by the participation dropping below 0.4. It is this phonon localization[32] that results in a sharp decrease in thermal conductivity, consistent with experimental observations and theoretical calculations of Anderson localization in disordered 2D systems[33].

Experimentally, we gather detailed information about excitations and phonon modes in both pristine and irradiated 2D-MoS_2. Figure 4d displays the Photoluminescence (PL) and Raman spectra of a pristine and irradiated (layer with nanopore) sheet of MoS_2. In the PL spectrum, the pristine flake exhibits a broad peak at 1.86 eV, where both the neutral (A^0) and charged (A^-) excitons contribute to the emission. The defected sheet is depicted with a deconvoluted spectrum, revealing defect-induced exciton peaks (X), along with weakly-trapped excitons, which are easily discernible. Moreover, some of the higher energy excitations become more prominent above 2.1 eV, possibly indicating Rydberg excited states arising from electron doping in the defect sites. The *E'* displacement mode is due to in-plane atomic vibrations of Mo and S atoms. The out-of-plane displacements mode (*A'*) for the irradiated film has a larger FWHM than the pristine flake, indicating a higher degree of localized strain. This is further evidenced by the relative displacement of the mode compared to the pristine flake. The disorder-induced edge that arises at ~ 378.0 cm^{-1} is attributed to the longitudinal optical (LO) mode splitting from the transverse optical (TO) mode.

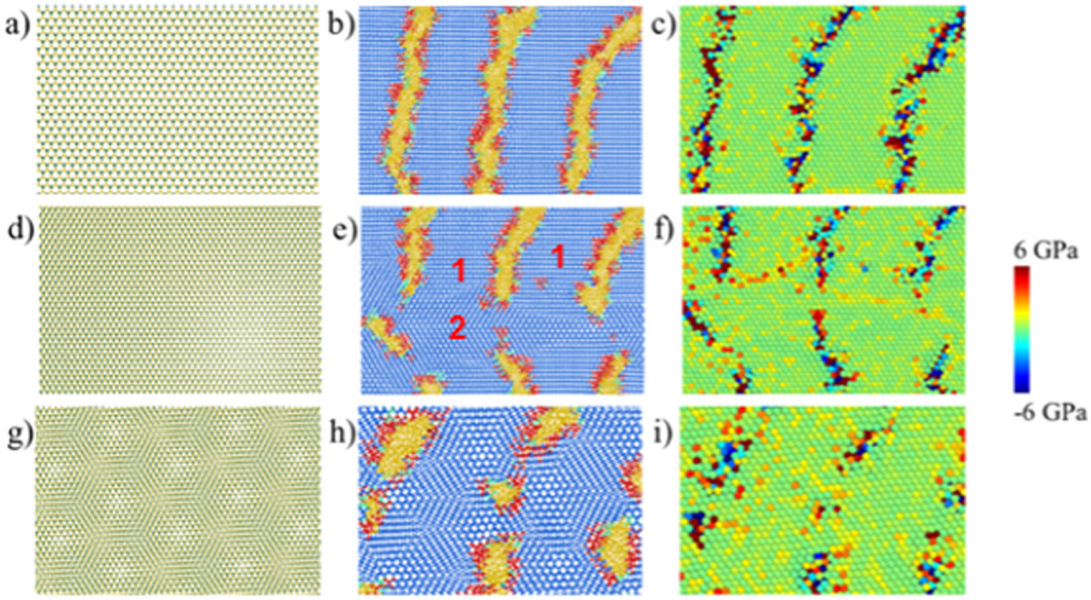

Fig. 5 | Shows defect generation and moiré patterns in the bilayer MoS_2 before and after the surface acoustic wave (SAW) passes through the constituent monolayers. Here we zoom in far from the nanopore region to show SAW-induced changes in the structure and stress distribution. The green atoms are Mo and yellow are S. The left column shows the initial structures, the middle column shows the changes in moiré pattern and defects, and the right column shows the stress distribution. The phases in the middle column are 2H (blue), α defect (red), and other defects (yellow). **a** shows the two layers in perfect registry as the relative twist between the two monolayers $\theta = 0°$. **b** shows the break in perfect registry when the SAW passes through the region and defects (red and yellow) form in regions of moiré patterns. **c** shows that stresses in defect regions are either very high or very low. **d**, **e** show the same phenomenon at $\theta = 0.5°$, where the moiré pattern have transformed (panel **e**), the regions between defects (marked as 1) have similar patterns and there is a horizontal region between two domains where there is a new moiré pattern (marked as 2). The corresponding stress distribution is shown in panel **f**. At $\theta = 5°$, the SAW propagation breaks the hexagonal moiré unit cells as shown in panels **g** and **h**. **i** shows the corresponding stress distribution.

SAW-induced moiré patterns in bilayers

MD simulations offer an atomistic perspective on defects generated by SAW propagation and changes in moiré patterns due to the relative rotation between the 2D-MoS_2 sheets in the bilayer system. The results are shown in Fig. 5, where we focus on regions far from the nanopore. The top, middle, and bottom rows correspond to twist angles $\theta = 0°$, 0.5°, and 5°, respectively. Panels in the left and middle columns show moiré patterns before and after SAW propagation, while the right column displays atomic-level stresses in the bilayer after SAW propagation. Prior to SAW propagation, the bilayers adopt the ground state 2H structure. However, after SAW propagation, we observe in panels (b), (e), and (h) phase transformation from 2H (blue) to α-defect (red) in regions exhibiting high out-of-plane displacements, as illustrated in Fig. 2. Chain-like defects labeled α (red) are under- and over-coordinated Mo atoms with 5 or 7S neighbors, and stresses in regions of α defects range between -6 GPa (tensile) and 6 GPa (compressive). In situ STEM data indicate that regions featuring α defects play a role in mediating transformations between semiconducting 2H and metallic 1 T phases in an MoS_2 monolayer[34]. In contrast, SAWs in an MoS_2 bilayer generate α defects between 2H structures.

We have investigated the structural and dynamical changes caused by the propagation of surface acoustic waves on both well-aligned and misaligned MoS_2 bilayers. Our precise experimental investigation of defect generation guides our simulation, ultimately unveiling that the structural features observed in experiments originate from the propagation of SAWs. HAADF-STEM images of irradiated single and bilayer MoS_2 sheets, coupled with MD simulations, reveal that SAWs originate in the flexible regions of nanopores within a single layer, subsequently inducing SAWs on the pristine MoS_2 layer positioned atop the monolayer containing the nanopore.

We have analyzed SAW propagation in MoS_2 bilayers with rotational misalignments ranging from 0.5° to 30°. We have provided a comprehensive explanation of how SAWs give rise to phonon focusing and how phonons are influenced by the presence of defects, such as nanopores. Out-of-plane atomic displacements and stress profiles reveal not only phonon-focusing phenomena but also cuspidal structures in well-aligned bilayers. Phonon focusing patterns degrade notably as the twist angle between the top and bottom layers increases.

By examining SAW velocity, we have determined the Young's modulus of an MoS_2 monolayer, which closely aligns with the experimental value. Moreover, SAW dynamics enable straightforward determination of thermal conductivity, with the computed values matching well with direct MD calculations, suggesting that the presence of nanopores dramatically reduces thermal conductivity by localizing low-energy phonon modes. Our combined experimental simulation study proposes that nanopore creation through strategic irradiation offers a facile means to modulate thermal transport, potentially creating highly insulating MoS_2 structures for energy storage applications.

Lastly, we have investigated SAW-induced structural changes in moiré patterns in MoS_2 bilayers, observing the formation of bands of line defects comprising under- and over-coordinated Mo atoms, which delineate crystalline 2H phases of MoS_2. These moiré patterns undergo significant changes with increasing misalignment between the bilayers, with the defect bands breaking up into smaller units of line defects.

Data availability

The datasets used and/or analyzed during the current study are available from the corresponding author on reasonable request.

Received: 5 December 2023; Accepted: 5 June 2024;
Published online: 28 June 2024

References

1. Ma, Q., Ren, G., Xu, K. & Ou, J. Z. Tunable optical properties of 2D materials and their applications. *Adv. Opt. Mater.* **9**, 2001313 (2021).
2. Delsing, P. et al. The 2019 surface acoustic waves roadmap. *J. Phys. D: Appl. Phys.* **52**, 353001 (2019).
3. Hernández-Mínguez, A., Liou, Y. & Santos, P. Interaction of surface acoustic waves with electronic excitations in graphene. *J. Phys. D: Appl. Phys.* **51**, 383001 (2018).
4. Bandhu, L. & Nash, G. R. Controlling the properties of surface acoustic waves using graphene. *Nano Res.* **9**, 685–691 (2016).
5. Huang, T. et al. Theoretical study on dynamic acoustic modulation of free carriers, excitons, and trions in 2D MoS2 flake. *J. Phys. D: Appl. Phys.* **50**, 114005 (2017).
6. Preciado, E. et al. Scalable fabrication of a hybrid field-effect and acousto-electric device by direct growth of monolayer MoS2/LiNbO3. *Nat. Commun.* **6**, 8593 (2015).
7. Rezk, A. R. et al. Acoustically-driven trion and exciton modulation in piezoelectric two-dimensional MoS2. *Nano Lett.* **16**, 849–855 (2016).
8. Burns, K. et al. Strain modulation using defects in two-dimensional Mo S 2. *Phys. Rev. B* **102**, 085421 (2020).
9. Krishnamoorthy, A. et al. Lattice thermal transport in two-dimensional alloys and fractal heterostructures. *Sci. Rep.* **11**, 1656 (2021).
10. Burns, K. et al. Controlling neutral and charged excitons in MoS2 with defects. *J. Mater. Res.* **35**, 949–957 (2020).
11. Hong, J. et al. Exploring atomic defects in molybdenum disulphide monolayers. *Nat. Commun.* **6**, 6293 (2015).
12. Zhou, W. et al. Intrinsic structural defects in monolayer molybdenum disulfide. *Nano Lett.* **13**, 2615–2622 (2013).
13. Burns, K. et al. Tailoring the angular mismatch in MoS2 homobilayers through deformation fields. *Small* **19**, 2300098 (2023).
14. Mann, J. et al. 2-Dimensional transition metal dichalcogenides with tunable direct band gaps: MoS2 (1–x) Se2x monolayers. *Adv. Mater.* **26**, 1399–1404 (2014).
15. Papadakis, E. P. *Physical acoustics.* Vol. 12. p. 277-374 (Elsevier, 1976).
16. Aussel, J.-D. & Monchalin, J.-P. Precision laser-ultrasonic velocity measurement and elastic constant determination. *Ultrasonics* **27**, 165–177 (1989).
17. Castagnede, B. et al. Determination of the elastic constants of anisotropic materials using laser-generated ultrasonic signals. *J. Appl. Phys.* **70**, 150–157 (1991).
18. Bayón, A. et al. Determination of the elastic constants of isotropic solids by optical heterodyne interferometry. *J. Acoust. Soc. Am.* **96**, 2589–2592 (1994).
19. Bayón, A. et al. Estimation of dynamic elastic constants from the amplitude and velocity of Rayleigh waves. *J. Acoust. Soc. Am.* **117**, 3469–3477 (2005).
20. Najafi, E. et al. Imaging surface acoustic wave dynamics in semiconducting polymers by scanning ultrafast electron microscopy. *Ultramicroscopy* **184**, 46–50 (2018).
21. Malischewsky, P. G. & Tuan, T. T. A special relation between Young's modulus, Rayleigh-wave velocity, and Poisson's ratio. *J. Acoust. Soc. Am.* **126**, 2851–2853 (2009).
22. Hess, P. Surface acoustic waves in materials science. *Phys. Today* **55**, 42–47 (2002).
23. Maznev, A., Kolomenskii, A. A. & Hess, P. Time-resolved cuspidal structure in the wave front of surface acoustic pulses on (111) gallium arsenide. *Phys. Rev. Lett.* **75**, 3332 (1995).
24. Sebastian, A. et al. Benchmarking monolayer MoS2 and WS2 field-effect transistors. *Nat. Commun.* **12**, 693 (2021).
25. Krishnamoorthy, A. et al. Evolutionary multi-objective optimization and Pareto-frontal uncertainty quantification of interatomic forcefields for thermal conductivity simulations. *Comput. Phys. Commun.* **254**, 107337 (2020).
26. Krishnamoorthy, A. et al. EZFF: Python library for multi-objective parameterization and uncertainty quantification of interatomic forcefields for molecular dynamics. *SoftwareX* **13**, 100663 (2021).
27. Mishra, A. et al. Multiobjective genetic training and uncertainty quantification of reactive force fields. *npj. Comput. Mater.* **4**, 42 (2018).
28. Rajak, P. et al. Autonomous reinforcement learning agent for chemical vapor deposition synthesis of quantum materials. *npj. Comput. Mater.* **7**, 108 (2021).
29. Ziegler, J. F., Ziegler, M. D. & Biersack, J. P. SRIM–The stopping and range of ions in matter (2010). *Nucl. Instrum. Methods Phys. Res. Sect. B: Beam Interact. Mater. At.* **268**, 1818–1823 (2010).
30. Vines, R., Tamura, S.-i & Wolfe, J. Surface acoustic wave focusing and induced Rayleigh waves. *Phys. Rev. Lett.* **74**, 2729 (1995).
31. Li, Y. et al. Mapping the elastic properties of two-dimensional MoS2 via bimodal atomic force microscopy and finite element simulation. *npj. Comput. Mater.* https://doi.org/10.1038/s41524-018-0105-8 (2018).
32. Luckyanova, M. N. et al. Phonon localization in heat conduction. *Sci. Adv.* **4**, eaat9460 (2018).
33. Anderson, P. W. Absence of diffusion in certain random lattices. *Phys. Rev.* **109**, 1492 (1958).
34. Lin, Y.-C. et al. Atomic mechanism of the semiconducting-to-metallic phase transition in single-layered MoS2. *Nat. Nanotechnol.* **9**, 391–396 (2014).

Acknowledgements

This work was supported by the National Science Foundation, Future Manufacturing Program, Award 2036359 and performed, in part, at the Center for Integrated Nanotechnologies, an Office of Science User Facility operated for the U.S. Department of Energy Office of Science. Sandia National Laboratories is a multi-mission laboratory managed and operated by National Technology & Engineering Solutions of Sandia, LLC, a wholly owned subsidiary of Honeywell International, Inc., for the U.S. DOE's National Nuclear Security Administration under contract DE-NA-0003525. A portion of this research was conducted at the Center for Nanophase Materials Sciences, which is a DOE Office of Science User Facility. A.A. acknowledges the funding from the US Department of Energy, Office of Science, Basic Energy Sciences, Award #DESC0019014 'Establishing defect-property relationships for 2D nanomaterials.'

Author contributions

Priya Vashishta, Rajiv Kalia, Aichiiro Nakano, and conceived the simulations. Kory Burns, Eric Lang, Jordan A. Hachtel, Khalid Hattar, and Assel Aitkaliyeva designed and carried out the experiments. Nitish Baradwaj, Ankit Mishra, and Anikeya Aditya performed simulations and data analysis. All authors wrote and reviewed the manuscript.

Competing interests

The authors declare no competing interests.

Additional information

Supplementary information The online version contains supplementary material available at https://doi.org/10.1038/s41524-024-01315-5.

Correspondence and requests for materials should be addressed to Rajiv Kalia.